

# Incorporating Tantalum Oxide Nanoparticles into Implantable Polymeric Biomedical Devices for Radiological Monitoring

Kendell M. Pawelec,\* Ethan Tu, Shatadru Chakravarty, Jeremy M. L. Hix, Lane Buchanan, Legend Kenney, Foster Buchanan, Nandini Chatterjee, Subhashri Das, Adam Alessio, and Erik M. Shapiro\*

Longitudinal radiological monitoring of biomedical devices is increasingly important, driven by the risk of device failure following implantation. Polymeric devices are poorly visualized with clinical imaging, hampering efforts to use diagnostic imaging to predict failure and enable intervention. Introducing nanoparticle contrast agents into polymers is a potential method for creating radiopaque materials that can be monitored via computed tomography. However, the properties of composites may be altered with nanoparticle addition, jeopardizing device functionality. Thus, the material and biomechanical responses of model nanoparticle-doped biomedical devices (phantoms), created from 0–40 wt% tantalum oxide (TaO<sub>x</sub>) nanoparticles in polycaprolactone and poly(lactide-co-glycolide) 85:15 and 50:50, representing non, slow, and fast degrading systems, respectively, are investigated. Phantoms degrade over 20 weeks in vitro in simulated physiological environments: healthy tissue (pH 7.4), inflammation (pH 6.5), and lysosomal conditions (pH 5.5), while radiopacity, structural stability, mechanical strength, and mass loss are monitored. The polymer matrix determines overall degradation kinetics, which increases with lower pH and higher TaO<sub>x</sub> content. Importantly, all radiopaque phantoms could be monitored for a full 20 weeks. Phantoms implanted in vivo and serially imaged demonstrate similar results. An optimal range of 5–20 wt% TaO<sub>x</sub> nanoparticles balances radiopacity requirements with implant properties, facilitating next-generation biomedical devices.

## 1. Introduction

The use of implanted biomedical devices has grown rapidly in recent decades. In particular, the application of polymers as medical devices has greatly increased, as a result of their excellent biocompatibility and materials properties including favorable mechanics and tunable biodegradation profiles. Despite their frequent use in the clinic, implants made from polymers fail for a number of reasons such as wear, tearing, migration, and infection.<sup>[1]</sup> With the inherent risk of failure following implantation of biomedical devices and to prevent situations that could irreparably impact patient health, there exists an increased need for a clinical methodology for in situ monitoring of device status following implantation.<sup>[1]</sup> However, for the majority of polymer implants, there is no robust endogenous contrast mechanism for clinical diagnostic imaging, and hence no mechanism for radiologists to diagnose problems prior to catastrophic failure. Incorporating radiological monitoring of biomedical devices as a standard part of surgical follow-up

 The ORCID identification number(s) for the author(s) of this article can be found under <https://doi.org/10.1002/adhm.202203167>

[+] Present address: TechInsights, Suite 500, 1891 Robertson Rd, Nepean, ON K2H 5B7, Canada

[++] Present address: Lake Erie College of Osteopathic Medicine, 1858 W Grandview Blvd, Erie, PA 16509, USA

© 2023 The Authors. Advanced Healthcare Materials published by Wiley-VCH GmbH. This is an open access article under the terms of the Creative Commons Attribution-NonCommercial-NoDerivs License, which permits use and distribution in any medium, provided the original work is properly cited, the use is non-commercial and no modifications or adaptations are made.

DOI: 10.1002/adhm.202203167

K. M. Pawelec, S. Chakravarty<sup>[+]</sup>, J. M. L. Hix, L. Buchanan, F. Buchanan<sup>[++]</sup>, N. Chatterjee, S. Das, A. Alessio, E. M. Shapiro  
Department of Radiology  
Michigan State University  
846 Service Rd, East Lansing, MI 48824, USA  
E-mail: paweleck@msu.edu shapir86@msu.edu

E. Tu, L. Kenney, A. Alessio  
Department of Biomedical Engineering  
Michigan State University  
775 Woodlot Dr, East Lansing, MI 48824, USA

J. M. L. Hix  
Institute for Quantitative Health Science and Engineering (IQ)  
Michigan State University  
775 Woodlot Dr, East Lansing, MI 48824, USA

A. Alessio  
Department of Computational Mathematics Science Engineering  
Michigan State University  
428 S. Shaw Ln, East Lansing, MI 48824, USA

could be a major step forward in the prevention of emergency interventions.

To impart contrast-generating properties into polymer devices requires modification of or incorporation of polymers with contrast agent specific to a clinical imaging modality.<sup>[2,3]</sup> Of these clinical modalities, computed tomography (CT) is a widespread technique that utilizes X-rays to form high-resolution 3D maps of tissue. A drawback to CT is that it cannot easily distinguish between different soft tissues with the same sensitivity as other imaging techniques, such as magnetic resonance imaging (MRI), and CT exposes patients to small amounts of radiation, which should be limited over a patient's lifetime.<sup>[4]</sup> However, for applications that require diagnosing implant damage, without concurrent interrogation of soft tissue status, the high clinical throughput, low cost, and favorable signal-to-noise ratio from surrounding tissue make CT beneficial for in situ monitoring.<sup>[3]</sup>

To utilize CT for monitoring polymeric biomedical devices, radiopacity must be introduced. Chemical modification of the polymer backbone has been proposed, but aside from changes to materials properties, there is the possibility of releasing cytotoxic elements during degradation.<sup>[5,6]</sup> Introduction of radiopaque nanoparticles is an extremely versatile alternative.<sup>[7,8]</sup> Tantalum oxide (TaO<sub>x</sub>) nanoparticles, in particular, are biocompatible in vivo with superior CT contrast over traditional iodinated compounds,<sup>[9,10]</sup> and can further be incorporated into polymeric matrices for use as biomaterials.<sup>[11,12]</sup> In our previous work, we proved that radiologists can identify location and device damage more successfully in phantoms incorporating TaO<sub>x</sub> nanoparticles than in polymer phantoms alone.<sup>[3]</sup> However, the incorporation of nanoparticles into polymeric devices requires a study on the impact of material properties that could alter device function, particularly as the percentage of nanoparticles increases. Specifically, imaging functionality should not interfere with the mechanical stability of devices while allowing tracking of features at a scale necessary to diagnose clinical outcomes.

In creating composite materials for biomedical devices, it is not only the incorporation of nanoparticles that can influence materials' properties but also the physiological environment of implantation. A particularly acidic environment, for example, one experiencing chronic inflammation or within a tumor,<sup>[13]</sup> may potentially accelerate the release of nanoparticles and induce local cytotoxicity. For this reason, the degradation of biomaterials after implantation has remained difficult to predict, even in systems where degradation mechanisms have been studied extensively.<sup>[14,15]</sup> Traditional degradation studies are conducted to simulate the physiological environment (saline, pH 7.4, 37 °C), but these have not proved predictive for the complex in vivo environment.<sup>[16]</sup> As in situ imaging relies on the sustained presence of nanoparticle contrast agents regardless of conditions, polymer degradation and potential nanoparticle release must be characterized in a comprehensive range of physiological environments, from lysosomal conditions (pH 5.5) to healthy tissue (pH 7.4).

The current study demonstrates the use of CT for in situ monitoring of model implantable biomedical devices (phantoms), over 20 weeks, using two of the most common polymers for manufacturing biomedical devices: polycaprolactone (PCL)<sup>[17]</sup> and poly(lactide-co-glycolide) (PLGA).<sup>[18]</sup> Hydrophobic TaO<sub>x</sub> nanoparticles were incorporated (0–40 wt%) into phan-

toms, as it has high radiopacity for their relative size and has been formulated to exhibit homogeneous mixing into hydrophobic polymer systems.<sup>[3,11]</sup> Phantoms were made using PCL, PLGA 50:50, and PLGA 85:15, mimicking porous isotropic scaffolds used for generic tissue engineering applications, covering the full range of predicted degradation behaviors from virtually non-degrading (years), slow degradation (months), and fast degradation (weeks).<sup>[15,17]</sup> Degradation in phantoms was characterized by tracking structural integrity, mechanics, mass loss, and radiopacity. Significant changes in degradation profiles were noted with buffer pH and TaO<sub>x</sub> incorporation, defining a practical limit of radiopaque contrast agent incorporation to guide future biomedical device design.

## 2. Results and Discussion

As the goal is to incorporate imaging functionality into implanted devices, radiopaque phantoms were manufactured to mimic state-of-the-art tissue engineering implants.<sup>[19,20]</sup> Specifically, the phantoms incorporated porosity at two different scales: macro-pores (200–400 μm) and micro-porosity (<100 μm), **Figure 1a–c**. The interconnected macro-porous structure is designed to facilitate processes like cellular infiltration and the micro-porosity contained within the pore walls can allow the diffusion of nutrients or chemokines within the structure. Both scales of porosity were introduced to FDA-approved biocompatible polymers using salt leaching, a process where polymer solutions are cast around water-soluble placeholders that are then removed to become pores, which is known to create interconnected and permeable implants.<sup>[19]</sup>

### 2.1. Radiopaque Polymer Matrices

Radiopacity was introduced to phantoms via the incorporation of hydrophobic TaO<sub>x</sub> nanoparticles (Figure 1e), with a nominal range of 0–40 wt% TaO<sub>x</sub>. The addition of nanoparticles to the matrices had no significant effect on the porous phantom structure (Figures S3–S4, Supporting Information). All phantoms had an interconnected porosity, with a mean pore size between 350 and 400 μm. A hydrophobic polymer coating on the TaO<sub>x</sub> particles allowed them to remain suspended and evenly dispersed in the polymer solutions during the manufacturing process. Micrographs of the pore walls show the even dispersion of the TaO<sub>x</sub> (Figure 1d), and the homogeneous dispersion ensured that no regions of the polymer matrices had significantly different material properties or X-ray attenuation. This was critical to ensuring a reproducible degradation profile throughout the structure and that any changes in phantom morphology over time could be observed.

Phantom radiopacity in saline buffer, visualized by micro-computed tomography (μCT), was dependent on the amount of TaO<sub>x</sub> incorporated into the polymer matrices, in agreement with the literature.<sup>[21–23]</sup> In μCT imaging, radiopacity depends on the ability of a material to attenuate incident X-rays.<sup>[24]</sup> The higher the concentration of elements, the greater the X-ray attenuation, and the higher the signal. The mass attenuation coefficient of the phantoms was dominated by the TaO<sub>x</sub> at the energies used for imaging (Figure S2, Supporting Information).

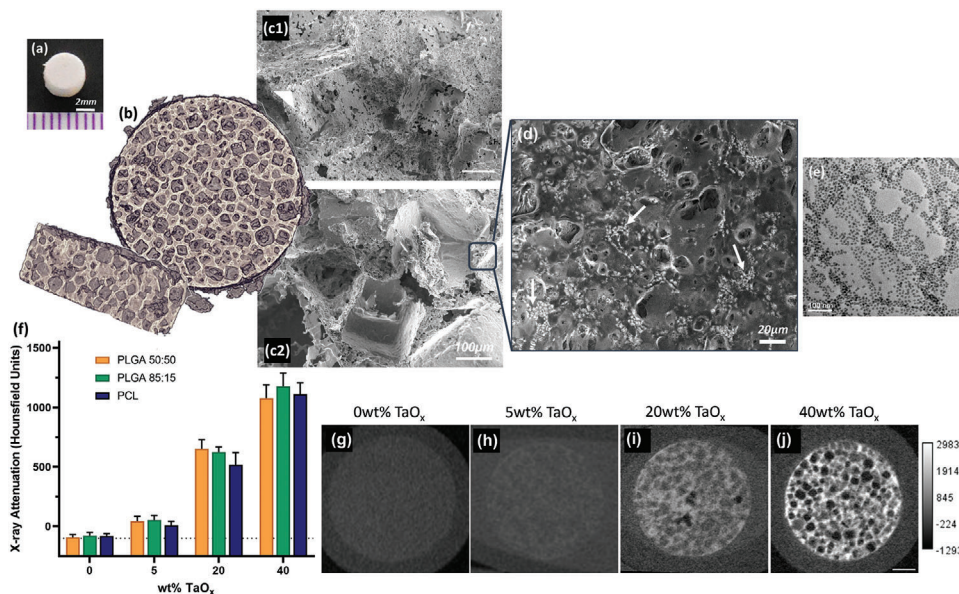


**Figure 1.** Radiopaque phantoms were produced to mimic key features of implantable biomedical devices. Porous phantoms were disks, as seen a) macroscopically, containing macro-porous features visible via b) 3D rendering of a  $\mu$ CT scan and c) in a corresponding scanning electron micrograph of the phantom cross-section: 1) 0 wt% TaO<sub>x</sub> nanoparticles, 2) 40 wt% TaO<sub>x</sub> nanoparticles. d) Radiopaque TaO<sub>x</sub> nanoparticles were homogeneously dispersed within the polymer matrix (white areas have a high TaO<sub>x</sub> concentration). e) TaO<sub>x</sub> nanoparticles at high magnification. f) X-ray attenuation was dependent on the amount of TaO<sub>x</sub> incorporated in the matrix, quantified from CT scans of phantoms with g) 0 wt% TaO<sub>x</sub>, h) 5 wt% TaO<sub>x</sub>, i) 20 wt% TaO<sub>x</sub>, and j) 40 wt% TaO<sub>x</sub>. The dashed line in (f) is the attenuation of blank media. The HU window is consistent for (g–j). Scale bar a) 2 mm, c) 100  $\mu$ m, d) 20  $\mu$ m, e) 100 nm, g–j) 1 mm.

In the case of porous materials like the phantom, the X-ray attenuation measured in the material was a mixture of the radiopaque matrix and the buffer that was trapped within the micro-porous walls. At 5 wt% TaO<sub>x</sub>, where phantoms were only just visible (Figure 1f–h), the radiopaque matrix could not be distinguished radiographically from the buffer, and the measured radiopacity is a combination of both. Thus, 5 wt% TaO<sub>x</sub> was determined to be the minimum addition that could still allow the gross phantom morphology to be distinguished in a hydrated environment. At higher weight percentages of TaO<sub>x</sub>, sufficient contrast existed between the matrix and the buffer (Figure 1i,j), that the micro-porous matrix could be radiographically distinguished from the aqueous media in the macro-pores and segmented by a semi-automated image analysis program. The upper range of TaO<sub>x</sub> was capped at 40 wt% to ensure that the polymer matrix was still the dominant phase within the phantoms. This range of radiopaque nanoparticles is in line with other studies utilizing elements such as gold<sup>[21]</sup> and gadolinium.<sup>[22]</sup> The true range of incorporation, after quantification via thermogravimetric analysis (TGA), was found to be 0–30 wt% TaO<sub>x</sub> (Figure S3, Supporting Information). The difference between theoretical and actual TaO<sub>x</sub> content is likely due to the loss of nanoparticles during the washing step of the leaching process. Regardless, phantoms made with different polymers did not have a significant difference in the amount of TaO<sub>x</sub> incorporated at each nominal value ( $\pm 0.5$  wt%), which was sufficient to make comparisons between the behavior of the phantoms based on nanoparticle addition.

Radiopacity has been imparted to phantom polymers through the incorporation of various elements including iodine,<sup>[23,25]</sup> gold,<sup>[21]</sup> barium sulfate (BaSO<sub>4</sub>),<sup>[26]</sup> and from other metal

oxides.<sup>[22]</sup> In cases of iodinated polymers, while high X-ray attenuation can be achieved, the phantom degradation rate increases with iodination leading to cytotoxicity in culture.<sup>[25]</sup> For nanoparticles, attenuation is dependent on the elements present. Gadolinium (Gd<sub>2</sub>O<sub>3</sub>) at 100 mm had >1000 HU,<sup>[22]</sup> while gold nanoparticles could achieve  $\approx 1000$  HU with 80 mm.<sup>[21]</sup> To achieve 1000 HU, required incorporation of at least 30 wt% TaO<sub>x</sub> nanoparticles utilized in this study. However, the TaO<sub>x</sub> can be produced at a lower cost than noble metals, like gold and platinum,<sup>[27]</sup> and does not have the cytotoxicity concerns of some metal oxides like bismuth<sup>[28]</sup> or the highly water-soluble nature of compounds, like BaSO<sub>4</sub>, that can limit their use with hydrophobic polymer matrices. In all cases, there exists a minimum amount of contrast agent needed to distinguish a phantom matrix from an aqueous media.

## 2.2. Degradation Profiles

Implantable biomedical devices are designed to support regenerating tissue during the initial stages of healing and should be engineered to degrade over time, allowing a new functional tissue matrix to replace the implant. Maintaining the structural integrity of the device during this time frame is essential, to ensure that infiltrating cells and capillaries are not dislodged or crushed during normal physiological movement of the patient. Defining the amount of time implanted devices must maintain integrity, and thus the corresponding optimal degradation rate for an implanted device is difficult as it depends on the location

of the implant, tissue to be regenerated, and overall size of the defect. Compounding the problem is that literature values for in vitro degradation tend to underestimate the in vivo degradation rate, despite being performed under simulated physiological conditions (phosphate-buffered saline [PBS], 37 °C).<sup>[16]</sup> These differences are due to the complexity of the in vivo extracellular environment, including blood/lymphatic flow and proteases, present within tissue. In addition, the in vivo environment is altered after surgical implantation due to acute inflammation processes, leading to local changes in pH and cell counts. Even when using well-characterized, FDA-approved biocompatible polymers, like PCL and PLGA, subtle changes like polymer end groups and chain length can affect the degradation rate and material properties of the implant during their degradation profile.<sup>[14,15,29]</sup> The addition of radiopaque nanoparticles to the polymer matrix also has the potential to change the degradation profile, and thus radiopacity of the matrix must be balanced along with other materials' properties.

The present study utilized phantoms from three biocompatible polymers that exhibited marked differences in degradation profile: non-degrading (PCL),<sup>[17]</sup> slow degrading (PLGA 85:15),<sup>[30]</sup> and fast degrading (PLGA 50:50).<sup>[16]</sup> This allowed the investigation and tracking of a full range of properties and behaviors and their time course. As observed in the current study, at one side of the spectrum, PCL with 0 wt% TaO<sub>x</sub> maintained structural integrity for a full 20 weeks, at physiological pH (7.4) and temperature (37 °C), where structural integrity is defined as maintenance of a micro-porous structure and >80% intact gross implant volume. Given the long time scale for PCL hydrolysis, macroscopic changes to PCL scaffolds around physiological pH generally do not occur prior to 6 months.<sup>[17]</sup> PLGA 85:15 also maintained structural integrity at 20 weeks, with 89.6 ± 5.4% of mass remaining. Only after 20 weeks have rapid and noticeable changes to PLGA 85:15 constructs been observed in standard physiological conditions.<sup>[30]</sup> Conversely, the structural integrity of PLGA 50:50 (0 wt% TaO<sub>x</sub>) was lost within 11 weeks, corresponding to >50% mass loss, in line with other reports on the degradation of isotropic porous devices.<sup>[16]</sup>

To begin to address the issues with extrapolation of in vitro degradation profiles to in vivo environments, phantoms (0–40 wt% TaO<sub>x</sub>) were further incubated under pH conditions that simulated chronic inflammation or tumor acidosis (sodium citrate, pH 6.5)<sup>[13,31]</sup> and cellular lysosomal conditions (sodium citrate, pH 5.5).<sup>[32]</sup> As expected, degradation was increased significantly at acidic pH due to the increased efficiency of hydrolysis reactions, responsible for the majority of degradation in PLGA and PCL.<sup>[14,17,33]</sup> The increase in the degradation rate was on the order of weeks, which was not noticeable for PCL within the 20-week period of the study, but significant for the fast-degrading PLGA 50:50, **Figure 2**. As seen visually in **Figure 2a,b**, structural integrity at pH 5.5 was lost several weeks before physiological pH. The visible trend correlated with accelerated mass loss in PLGA 50:50 at pH 5.5 compared to pH 6.5 or 7.4, **Figure 2d–f**. The effects of buffer pH were maintained regardless of the amount of TaO<sub>x</sub> included in the phantom. Since the radiopaque element did not alter the basic response of the matrices to buffer pH, there is potential to gain a critical real-time assessment of matrix degradation. This may prove particularly important for “smart” devices that are designed to allow drug release during matrix dissolution,

particularly in microenvironments where pH may not be definitively known such as in tumors where acidosis is prevalent.<sup>[31]</sup>

Not only are structural integrity and matrix mass important to understanding device degradation, but mechanical properties are also key for device function. Both PLGA 50:50 and 85:15 phantoms had significantly higher mechanical strength, measured as a compressive modulus, than PCL initially. Over time, the effects of the buffer pH became far more significant in determining the overall mechanical behavior. In all cases of TaO<sub>x</sub> incorporation into the phantoms, mechanical stability was lost first at the lowest pH, consistent with the accelerated mass loss. With a high level of porosity within phantoms, the mechanical strength reported is an apparent strength of the structure rather than a true material property of the matrix. When exposed to compressive loading, structural collapse of hydrated scaffolds occurs in stages, starting with reversible deformation of the porous walls (giving an apparent compressive modulus), followed by a collapse of the macro-porous structure and further densification of the remaining micro-pores. As this apparent modulus is dependent on the porosity within the structure, any changes to the apparent density from the degradation process affect the compressive modulus.<sup>[30]</sup> In particular, PLGA 50:50 experienced the greatest increases in apparent compressive modulus during degradation due to macroscopic changes in overall volume, **Figure 3**, that were influenced by the buffer pH, but PLGA 85:15 also experienced significant increases in strength over the first 10 weeks as well. While PCL had the lowest apparent modulus, mechanical strength was maintained over the 20-week period.

Deformation is another feature of devices affecting overall functionality, particularly in cases when devices are implanted in high-stress environments, where large deformations after mechanical loading correlate to a permanent loss of a device's prestressed shape and potentially catastrophic failure. The deformation of the phantoms, measured as the recovery of phantom thickness after compression,<sup>[34]</sup> was dependent on both the polymer matrix and the pH of the buffer. Deformation of PCL phantoms was consistently around 20%, demonstrating a high level of compliance and recovery. In contrast, PLGA phantoms behaved as brittle materials, with very little recovery in the micro-porous structure.<sup>[34]</sup> In general, deformation tended to increase as densification of the scaffold occurred, particularly at low pH, and changed significantly as the mechanical strength was lost, **Figure 4d–f**.

Importantly for understanding degradation profiles of biomedical devices, different metrics responded at significantly different time scales. Large percent differences between measured mass loss and the volume of the phantom matrix were observable over 20 weeks, **Figure 2g,h**, due to macroscopic swelling or shrinkage of the phantoms over time. Also, phantoms from PLGA 50:50 demonstrated a consistent loss of mechanical stability without a correspondingly significant change in mass loss, **Figure 4**. Both mass loss and mechanics are often reported as measures of matrix stability during degradation, but there is little predictive value between them. Indeed, the processes governing the two metrics are different. Mechanical strength is affected by the cleavage of polymer chains within the porous structure, and in this case, significant changes to apparent density. However, the mass loss has been compared to an erosion process, which is dependent on both cleavages of

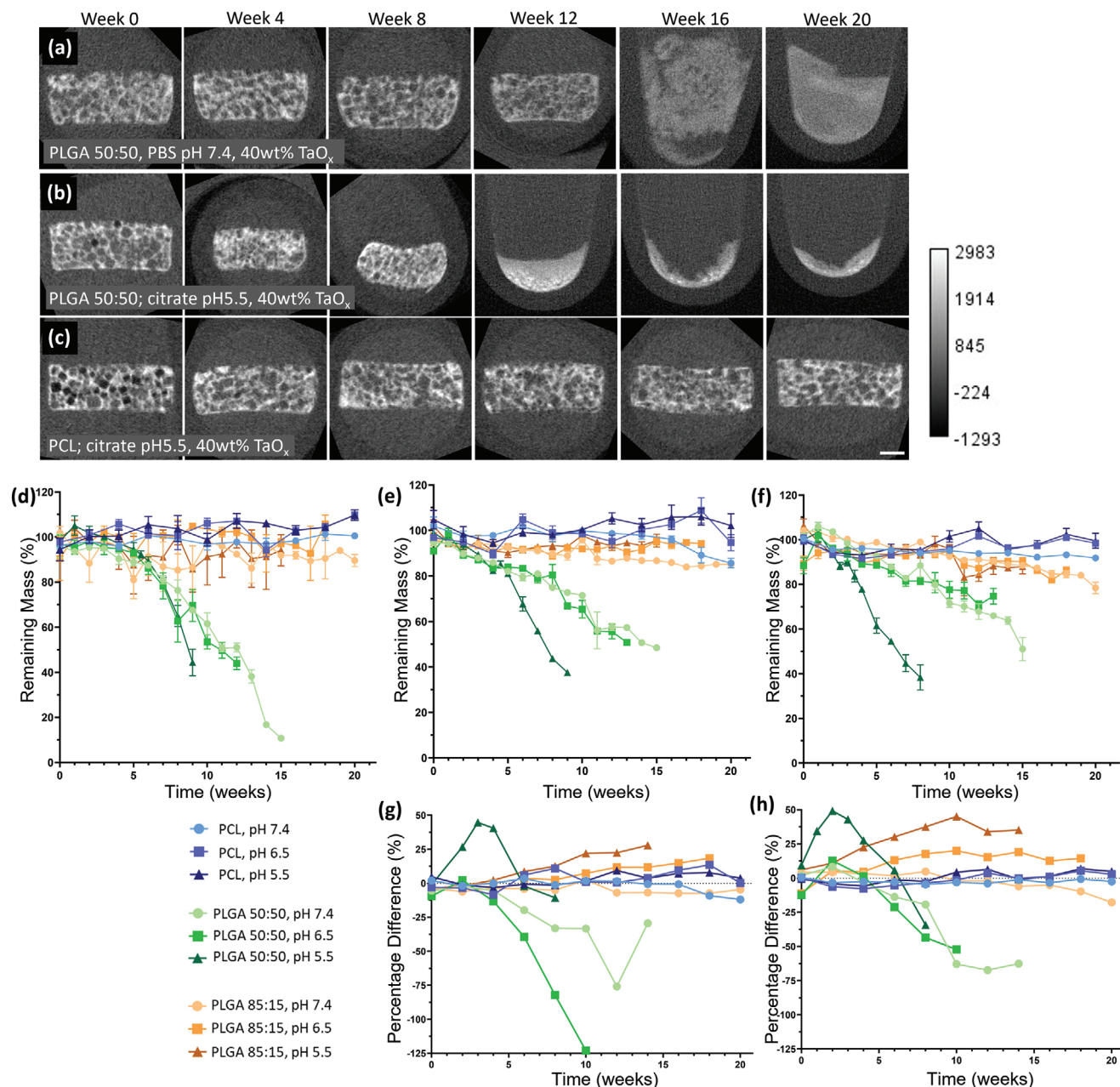


**Figure 2.** The structural integrity of phantoms over time was largely determined by the matrix polymer but was lost earlier in lower pH environments. The effects were most noticeable in fast degrading polymers compared to non-degrading polymers, as seen visually in  $\mu$ CT reconstructions over 20 weeks for: a) PLGA 50:50 + 40 wt% TaO<sub>x</sub> at pH 7.4, b) PLGA 50:50 + 40 wt% TaO<sub>x</sub> at pH 5.5, and c) PCL + 40 wt% TaO<sub>x</sub> at pH 5.5. Mass loss mirrored the trends in structural integrity and was consistent regardless of TaO<sub>x</sub> incorporation: d) 0 wt% TaO<sub>x</sub>, e) 20 wt% TaO<sub>x</sub>, and f) 40 wt% TaO<sub>x</sub>; data presented as mean  $\pm$  SEM. The percent difference between mass and matrix volume was affected by changes in scaffold dimension for g) 20 wt% TaO<sub>x</sub> and h) 40 wt% TaO<sub>x</sub>; graphs plot the percent difference between group averages. Positive differences represent cases where the matrix volume decreases and negative values represent cases where the matrix volume increases. Scale bar (a–c): 1 mm; HU window is consistent.

polymer chains within the structure and the diffusion of material from the implant itself.<sup>[14]</sup> Thus, the solubility of degradation products, swelling, and surface area can all affect mass loss in ways that may not be as important for mechanical integrity.<sup>[14]</sup>

While trends in the buffer pH on degradation remained consistent regardless of nanoparticle incorporation, the addition of nanoparticle fillers into polymer matrices is also known to in-

dependently affect the mechanical strength and degradation of composite matrices.<sup>[35]</sup> In the case of the porous phantoms, there were trends in the compressive modulus of the matrices, as the TaO<sub>x</sub> content increased to 40 wt%. In a PCL matrix, the nanoparticles tended to create a stiffer matrix, likely hindering the sliding of polymer chains within the pore walls; the apparent modulus of the phantoms went from  $2.59 \pm 1.2$  to  $4.51 \pm 2.7$  kPa with 0 and

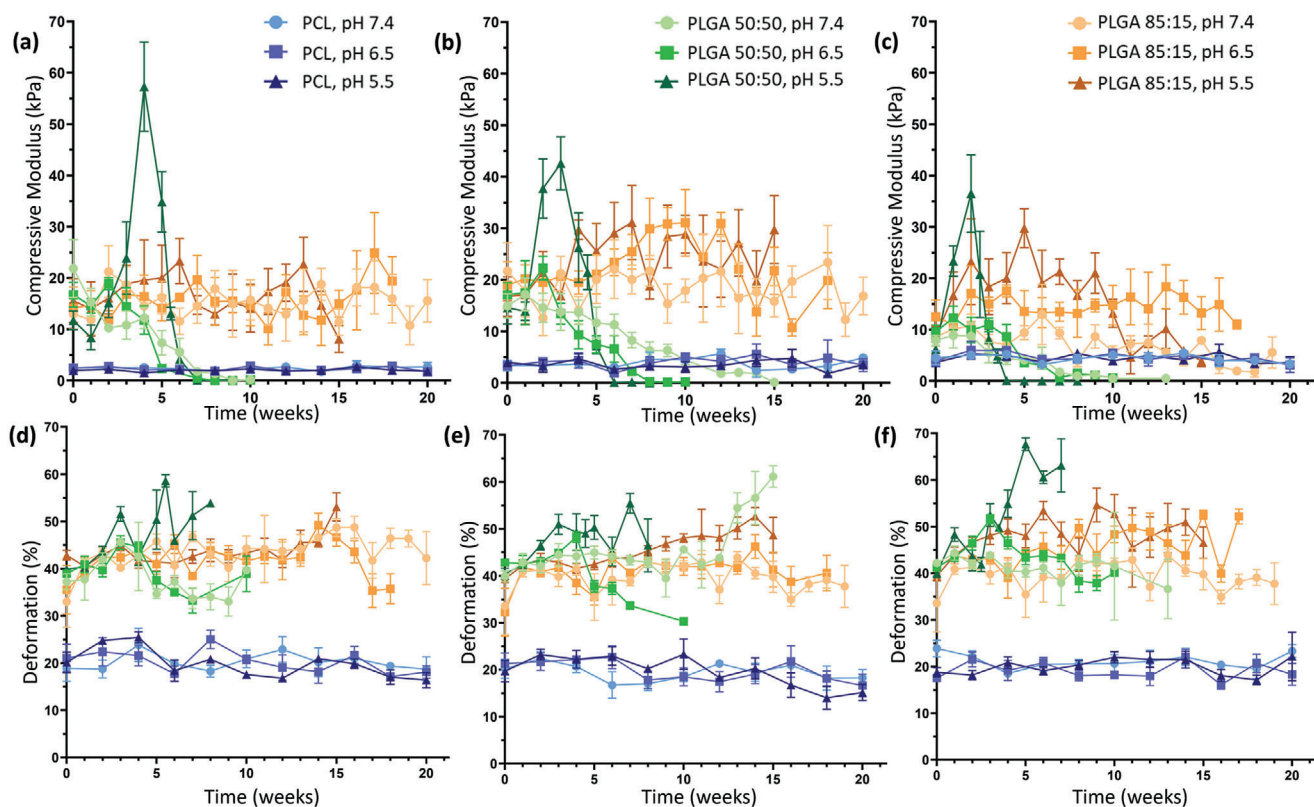


**Figure 3.** The polymer matrix in the porous phantoms drove the mechanical behavior, as measured by a–c) apparent compressive modulus and d–f) deformation. The pH of the buffer had a significant impact on mechanical properties at all levels of TaO<sub>x</sub> incorporation: a, d) 0 wt% TaO<sub>x</sub>, b, e) 20 wt% TaO<sub>x</sub>, and c, f) 40 wt% TaO<sub>x</sub>. Data reported as mean ± SEM.

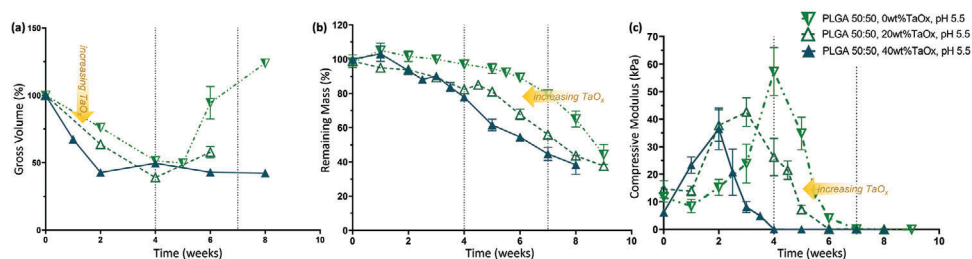


**Figure 4.** TaO<sub>x</sub> incorporation increased phantom hydrolysis in fast-degrading PLGA 50:50. At pH 5.5, increased wt% TaO<sub>x</sub> sped up the rate of a) initial volume change, b) mass loss, and c) loss of compressive modulus over time. Metrics for quantifying degradation do not share the same features. Data reported as mean ± SEM.

40 wt%, respectively. In contrast, both types of PLGA matrices had reduced mean compressive modulus as the incorporation of TaO<sub>x</sub> increased from 20 wt%; the apparent modulus decreased by up to half for PLGA 50:50 ( $15.91 \pm 11.05$  to  $7.90 \pm 1.99$  kPa). Interactions between the polymer chains and the hydrophobic layer around the nanoparticles may not allow entanglement of the individual polymer chains, thus facilitating the movement of the pore walls. Despite the trends, the effect of the porosity on the phantom modulus, both micro and macro, created too much variation for statistical significance.

Effects from TaO<sub>x</sub> incorporation over time appeared to be mediated by increased water penetration into the polymer matrix

of the phantoms, increasing hydrolysis reactions. In the case of PLGA 50:50, all metrics describing scaffold integrity and mechanical stability experienced a faster decline with increased weight percent of TaO<sub>x</sub>, Figure 4. Loss of mechanical strength for PLGA 50:50 at pH 5.5 occurred after 4 weeks for 40 wt% TaO<sub>x</sub> as opposed to 7 weeks for native polymer (0 wt% TaO<sub>x</sub>), Figure 4c. In PLGA 85:15, increased hydrolysis correlated to an increase in the rate of volume changes within the scaffold matrix, if not a clear correlation with loss of mechanics. PCL phantoms, in contrast, appeared largely unaffected by the addition of nanoparticles. In other systems, PCL composite materials have been shown to have increased degradation rates, due to the added

intercalation of water within the matrix, effectively increasing the surface area available for hydrolysis.<sup>[35]</sup> However, in these studies, the size of the particles and porosity of the matrix was completely different, making direct comparison difficult.

From the present study, it is clear that degradation is largely controlled by the polymer matrix used to create the phantom. Local environmental factors, such as pH, played a much larger role in accelerating degradation processes than the addition of radiopaque nanoparticles. Considering the traumatic environment encountered by biomedical devices upon implantation, further acceleration of degradation with large amounts of TaO<sub>x</sub> (40 wt%) would likely be impractical for most applications, creating an effective upper limit on TaO<sub>x</sub> incorporation. The TaO<sub>x</sub> nanoparticles would likely shorten PCL degradation time as well, but whether on the order of weeks or months is currently unclear.

### 2.3. Longitudinal Monitoring

Translating longitudinal monitoring to the clinic successfully requires the ability to clearly track changes in biomedical devices over time, despite damage or disease in surrounding tissues. Thus, any potential monitoring paradigms must be robust during both mechanical failure, device movement, and degradation, which represent common failure mechanisms of biomedical devices in diverse areas from hernia patches to knee replacement.<sup>[1,36,37]</sup> With the promising results on phantom radiopacity at initial time points, we further demonstrated that the incorporation of TaO<sub>x</sub> nanoparticles resulted in radiopaque phantoms that could be imaged through a 20-week time course, Figure 2. Importantly, the TaO<sub>x</sub> appeared to remain associated with the polymer matrix, despite the loss of structural integrity of the phantoms, allowing for real-time characterization of the phantoms which could corroborate the data on mechanical properties and mass loss.

Since the X-ray attenuation over time was dependent on the amount of TaO<sub>x</sub> present in the matrix, only the gross volume, or the volume occupied by a solid cylinder with the corresponding outside thickness and diameter measured by CT, could be recorded for phantoms with 5 wt% TaO<sub>x</sub>, Figure 5d,e1,f1. Even from the gross volume alone, very clear trends in the phantom volume changes over the degradation period were visible. The changes in volume were driven primarily by the buffer media and from degradation products, such as lactic acid, which could affect the environment within the phantom itself.<sup>[14]</sup> It is well known that PLGA will experience bulk degradation, caused by the breakdown of the glycolic acid chain and release of lactic acid that has auto-catalytic activity by lowering the local pH within porous structures.<sup>[38]</sup> As expected, with its high glycolic acid content, PLGA 50:50 was far more affected during degradation than PLGA 85:15, evidenced by drastic changes in gross volume.<sup>[16]</sup> At a buffer pH of 5.5, PLGA 50:50 rapidly contracted to <50% of its original gross volume, consistent with other studies that note volume decreases coincident with pH drops within devices during degradation.<sup>[30]</sup> In this case, the buffer was responsible for the acid environment rather than the acid by-products of degradation. Conversely, at a buffer pH of  $\geq 6.5$ , PLGA 50:50 phantoms tended to swell. It has been hypothesized that the internal build-up of acidic by-products encourages water infiltration into PLGA

structures and relaxation of the polymer matrix which further drives the swelling behavior.<sup>[38]</sup> Peak swelling occurred at pH 6.5, reaching >250%, >600%, and >150% of the original scaffold volume for 5, 20, and 40 wt%, respectively. These extreme values for swelling are likely underestimated for 5 wt%, as the analysis was conducted on CT scans, and 5 wt% could not be distinguished from the background after 6 weeks, even for gross volume calculations. CT scans of the radiopaque PLGA 50:50 noted the development of cavitation in the interior of the phantom matrix over time at pH 6.5 and 7.4, while the outer surface remained intact. This is typical of internal bulk degradation of PLGA constructs, where there is a little outward indication of the loss of structural integrity from macroscopic observation.<sup>[14]</sup> Like PLGA 50:50, PLGA 85:15 phantoms also underwent significant volume changes, namely contraction, over the study period, which was most evident at pH 5.5. A typical time frame for PLGA 85:15 devices to exhibit gross morphology changes is around 19–24 weeks, in line with the current study.<sup>[16,30]</sup>

The effect of degradation on the porous structure could be examined more closely in phantoms with >5 wt% TaO<sub>x</sub>, as the volume of the matrix could be separated from the internal macropores. Percent porosity, related to the macropores within the phantom, was calculated as the percentage of the gross volume not occupied by the matrix. Prior to degradation, all scaffolds with 20 wt% TaO<sub>x</sub> had between 30% and 40% porosity, and all 40 wt% TaO<sub>x</sub> phantoms had a 20–30% porosity, Figure 5e2,f2. The difference between the two groups in initial porosity is an overestimation of the matrix volume during the segmentation process, the result of balancing the threshold for the program to distinguish matrix from background consistently through the entire series of phantoms. From the percentage porosity, it was clear that swelling of PLGA 50:50 at pH 6.5 increased the internal porosity significantly, while the densification of phantoms at pH 5.5 appeared to be driven by a decrease in open pore volume over and above decreases in polymer matrix volume. This implies a restriction of nutrient or fluid flow through the porous phantoms as degradation progresses or even a total collapse of porosity in the worst-case scenario. The extreme contraction of porous devices during cellular infiltration has been tied to poor repair outcomes, necessitating research into ways to resist contractile forces.<sup>[39,40]</sup> Swelling, on the other hand, is not likely to interfere with tissue repair, as biomedical implants are generally constrained by surrounding tissues after implantation. Swelling might, however, influence the diffusion of drugs or therapeutics from a polymer matrix.<sup>[38]</sup>

As observed in the initial characterization of radiopaque phantoms, the X-ray attenuation was dependent on the amount of TaO<sub>x</sub> present in the matrix. While the matrix remained at a constant volume, as was the case for PCL throughout the study, the X-ray attenuation remained unchanged. On the other hand, as PLGA matrices contracted or expanded, the X-ray attenuation of the phantoms inversely increased and decreased, Figure 5e3, f3. This is largely due to the apparent concentration of the contrast agent, TaO<sub>x</sub> in this case, within the matrix. As there was no significant change in TaO<sub>x</sub> amount, movement of the matrix either concentrated or diluted the nanoparticles which were available to attenuate X-rays. At pH 6.5, PLGA 50:50 with 5 or 20 wt% TaO<sub>x</sub> expanded to such an extent (Figure 5d1,e1) that there was no longer sufficient contrast to either visualize the scaffold or

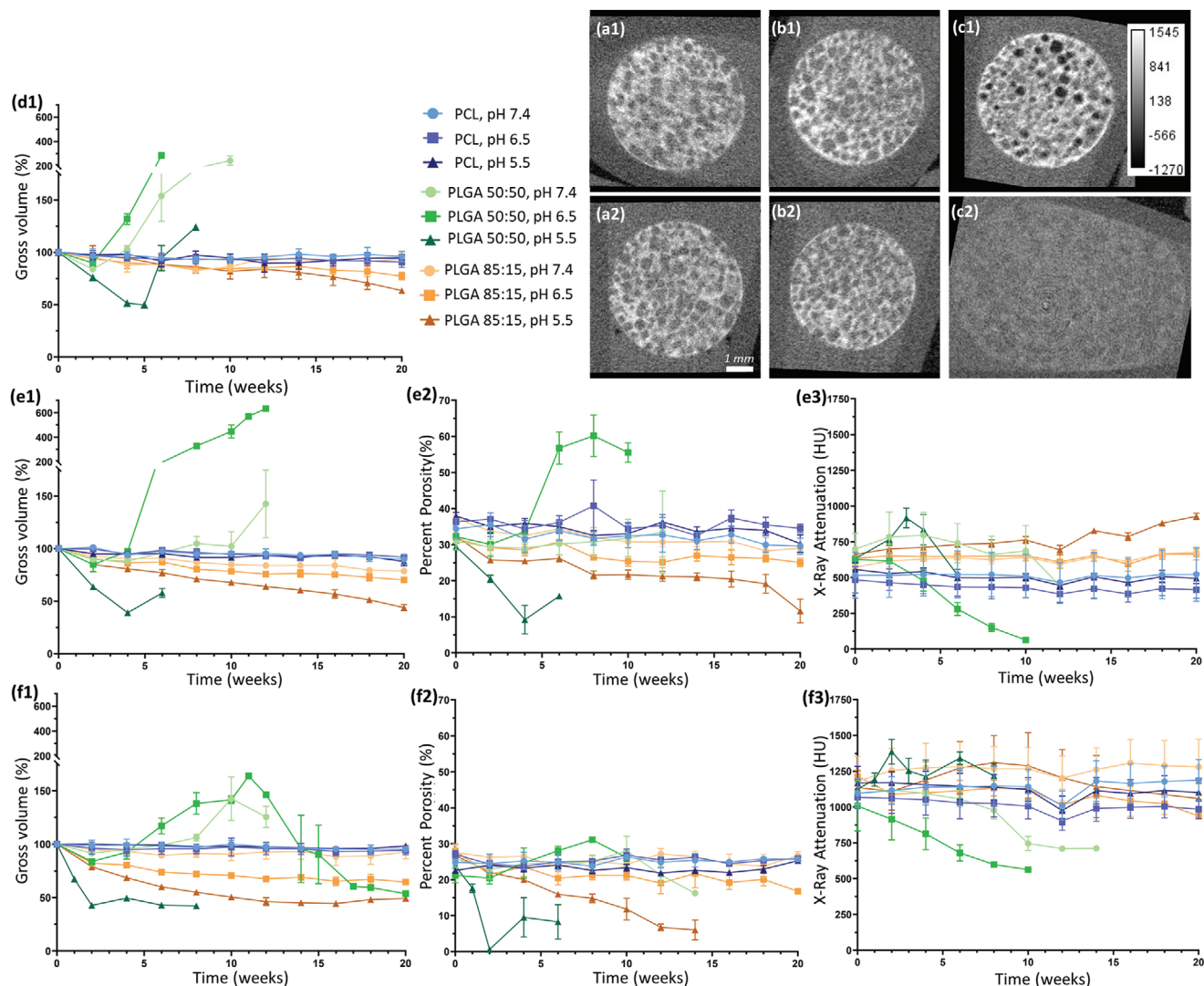


**Figure 5.** Phantoms with TaO<sub>x</sub> nanoparticles could be monitored for 20 weeks without loss of radiopacity due to particle leaching. a–c) This allowed for visual monitoring of changes to phantom shape and porosity, as illustrated by CT images from 1) day 1 and 2) 6 weeks: a) PCL+20 wt% TaO<sub>x</sub>, b) PLGA 85:15 + 20 wt% TaO<sub>x</sub>, and c) PLGA 50:50 + 20 wt% TaO<sub>x</sub>. During degradation, significant changes occurred within the phantoms: 1) gross phantom volume, 2) percentage porosity, and 3) X-ray attenuation. TaO<sub>x</sub> incorporation ranged from d) 5 wt% TaO<sub>x</sub>, e) 20 wt% TaO<sub>x</sub>, and f) 40 wt% TaO<sub>x</sub>. At 5 wt% TaO<sub>x</sub>, only the gross volume of the phantoms could be quantified, as the matrix could not be segmented from the background. Scale (a–c): 1 mm; HU window is consistent for all images. Data reported as mean ± SEM.

segment the matrix from the buffer, due to the drop in attenuation. In contrast, at pH 5.5, PLGA 50:50 phantoms showed increases in phantom attenuation before the structural integrity was lost, Figure 5e3,f3. Even after integrity was lost, enough TaO<sub>x</sub> remained associated with the polymer to distinguish the remains of the phantom structure from the surrounding environment, Figure 2b.

As in the case of phantom mechanics, nanoparticle incorporation had an independent effect of the buffer pH on volume changes. Overall, higher percentages of TaO<sub>x</sub> tended to lower the overall volume of the phantom. This manifested as either an increasing phantom contraction or decreased swelling. In PLGA phantoms, this also manifested as an increase in the rate of volume change, most apparent for PLGA 85:15. With the known bulk degradation mechanism of PLGA, the higher levels of TaO<sub>x</sub>

may limit the build-up of acidic degradation products within the scaffold core, which has shown to be tied to swelling kinetics in PLGA microspheres.<sup>[38,41]</sup> The nanoparticles may be contributing by limiting the amount of degradation product available overall or by increasing the hydrolysis of the polymer matrix to allow the escape of acidic groups before significant build-up.

Within the *in vitro* microenvironment, the nanoparticles remain associated with the matrix rather than remaining suspended in the degradation buffer, likely due to the hydrophobic nature of the polymer and nanoparticles. During *in vivo* degradation, both polymer degradation products (monomers, oligomers) and TaO<sub>x</sub> nanoparticles are expected to behave in a similar manner. They must diffuse to the blood, after which they can be excreted via the liver, kidneys, and spleen.<sup>[9,42]</sup> For nanoparticles, clearance has been shown to go rapidly from the blood,

with less than 1.15% injected dose remaining in the body after 48 h.<sup>[9]</sup> Previous *in vivo* nanoparticle studies have not demonstrated any blurring of device features during sequential CT scans due to dispersed nanoparticles, so the results in long-term monitoring should be consistent with the data collected during *in vivo* applications.<sup>[22]</sup>

The incorporation of nanoparticles within slow-degrading polymer matrices is a way to conveniently localize radiopaque markers or implants, bypassing the immediate problems with cellular toxicity of concentrated nanoparticle bolus injections and providing a sustained signal.<sup>[11,21,22]</sup> Introducing radiopacity to implantable devices is a facile and flexible way of monitoring and predicting implant failure, particularly where local tissue environments are in flux due to trauma or disease.<sup>[3]</sup> A range of 5–20 wt% TaO<sub>x</sub> appears optimal for synthetic biodegradable scaffolds, enabling visualization without significantly impairing mechanical properties. Due to differences in inflammatory responses and mechanical forces at different implantation sites, the physiological environment for every implant is expected to be slightly different. Thus, having information on the full range of potential degradation profiles is critical for the rational design of next-generation implants. Differential location within the body is not a concern for CT imaging, as penetration of high-energy X-rays has excellent resolution with no limitations on penetration depth.<sup>[2]</sup> Indeed, phantoms with 20–30 wt% TaO<sub>x</sub> could be implanted and successfully monitored when placed subcutaneously, intraperitoneally, and intramuscularly in a rodent model, **Figure 6**, and movement over time of the implants could be easily tracked (**Figures S5–S7**, Supporting Information). Higher-resolution scans also allowed for finer phantom features to be identified. This clearly offers the flexibility needed for biomedical implants, while working within already-established clinical workflows for imaging patients.

### 3. Conclusions

Radiopaque implantable devices offer the potential to monitor the real-time response of polymeric devices to their environment and to predict device failure, both during the device development phase and in the clinic. Hydrophobic radiopaque TaO<sub>x</sub> nanoparticles were incorporated homogeneously within a variety of biocompatible polymer phantoms, with 5 wt% TaO<sub>x</sub> being the minimum to enable *in situ* monitoring of gross phantom features (overall volume, location) using  $\mu$ CT. Beyond 20 wt% TaO<sub>x</sub>, there was a limited advantage in terms of imaging, and increasing destabilization of the polymer matrix. Importantly, within this range of 5–20 wt%, the radiopacity of phantoms was maintained over 20 weeks. Phantom X-ray attenuation was impacted most significantly by swelling and contraction during degradation, which essentially diluted or concentrated the contrast agent. The overall degradation profile of phantoms was dictated by the polymer matrix. Lower pH environments and high nanoparticle content (>20 wt% TaO<sub>x</sub>) increased hydrolysis, simultaneously increasing degradation rate, as measured by mass loss, structural integrity, and mechanical stability. This study demonstrates comprehensive testing of phantom degradation profiles with simultaneous imaging, representing a significant step toward incorporating *in situ* monitoring into the next generation of implantable devices.

### 4. Experimental Section

**Materials:** The study utilized three types of biocompatible polymers: PCL, PLGA 50:50, and PLGA 85:15. PCL (Sigma Aldrich) had a molecular weight average of 80 kDa. PLGA 50:50 (Lactel/Evonik B6010-4) and PLGA 85:15 (Expansorb DLG 85–7E, Merck) were both ester terminated and had a weight average molecular weight between 80 and 90 kDa, to minimize the effects of polymer chain length on the degradation rate.<sup>[14]</sup>

**Hydrophobic TaO<sub>x</sub> Nanoparticles:** Hydrophobic TaO<sub>x</sub> nanoparticles were manufactured based on the previous procedure with one minor change.<sup>[11]</sup> Hydrophobicity was imparted by coating nanoparticles with aliphatic organosilanes. Here, the organosilane used was hexadecyltriethoxysilane (HDTES, Gelest Inc, cat no SIH5922.0) rather than (3-aminopropyl) trimethoxy silane (APTMS, Sigma). The TaO<sub>x</sub> nanoparticles were spherical, 3–9 nm in diameter (Supplemental data). The weight percentage (wt%) of TaO<sub>x</sub> in dichloromethane (DCM, Sigma) was determined by TGA; this was used to calculate the wt% of TaO<sub>x</sub> theoretically incorporated into phantoms.

**Phantom Manufacture:** Phantoms were created with micro-scale porosity (<100  $\mu$ m) and with macro-scale porosity (200–500  $\mu$ m) to mimic tissue engineering constructs which must accommodate both nutrient diffusion and cell and tissue infiltration. A detailed protocol for preparing polymer slurries is in the Supporting Information. Briefly, biocompatible polymers were solubilized in suspensions of TaO<sub>x</sub> nanoparticles in DCM; solutions were 8 and 12 wt% for PCL and PLGA, respectively. TaO<sub>x</sub> suspensions were calculated so that the final phantom mass (polymer + nanoparticles) would consist of 0–40 wt% TaO<sub>x</sub>. Sucrose (Meijer) was added to the suspension, calculated to be 70 vol% of the polymer + nanoparticle mass in solution, followed by NaCl (Jade Scientific) at 60 vol% of the total polymer + nanoparticle volume. The suspension was vortexed for 10 min and pressed into a silicon mold that was 4.7 mm diameter, and 2 mm high. After air drying, phantoms were removed, trimmed of excess polymer, and then washed for 2 h in distilled water, changing the water every 30 min to remove sucrose and NaCl. Washed phantoms were air-dried overnight and stored in a desiccator prior to use.

**Scanning Electron Microscopy:** Samples were adhered to 13 mm aluminum stubs and sputter coated with platinum. Surfaces were examined using a Zeiss Auriga, at 7 keV in scanning electron mode, and 20 keV for backscatter electron images.

**Thermogravimetric Analysis:** TGA was used to characterize the wt% of TaO<sub>x</sub> nanoparticles in DCM after manufacture and the final wt% of TaO<sub>x</sub> incorporated into polymeric phantoms. To determine initial wt% TaO<sub>x</sub>, the DCM solution was massed in an alumina pan and allowed to dry before placing it in a TA Q500 (TA Instruments). For wt% TaO<sub>x</sub> in phantoms, 12–14 mg of dry material was massed in an alumina pan. Samples were then heated to 600 °C at a rate of 10 °C min<sup>-1</sup> under a nitrogen environment. The percentage of nanoparticles was calculated as the difference between the initial and final mass; for solutions, the initial mass was the mass of the DCM solution added to the pan.

**Degradation Study:** An *in vitro* degradation study was performed to assess the effects of the TaO<sub>x</sub> incorporation on device properties. Three buffers were used, to simulate a range of physiological conditions: pH 7.4 PBS (Thermo Fisher Sci), pH 6.5 0.05 M sodium citrate (Thermo Fisher Sci), and pH 5.5 0.05 M sodium citrate (Thermo Fisher Sci). Dry phantoms were placed into individual, pre-weighed, microcentrifuge tubes. Phantoms were hydrated on day 0, by adding 1 mL buffer and centrifuging for 10 min at 11 000 rpm. Afterward, immersed phantoms were stored at 37 °C, and the buffer was changed weekly. Phantoms with 0, 20, and 40 wt% TaO<sub>x</sub> were tested for mechanics and mass loss ( $n = 4$  per time point). A further cohort of phantoms ( $n = 3$ ) containing 5, 20, and 40 wt% TaO<sub>x</sub> were serially imaged via  $\mu$ CT, to follow the degradation process and assess radiopacity over time.

**Mechanics and Mass Loss:** Prior to performing mechanical tests, phantom thickness and diameter were measured using a micrometer. Phantoms were loaded onto a TAXT plus Texture analyzer (Stable Micro Systems) with a 5 kg load cell, compressed to 40% of their original thickness, at 1 mm min<sup>-1</sup> and then unloaded. The loading cycle was repeated twice. The compressive modulus was calculated as the initial slope of the

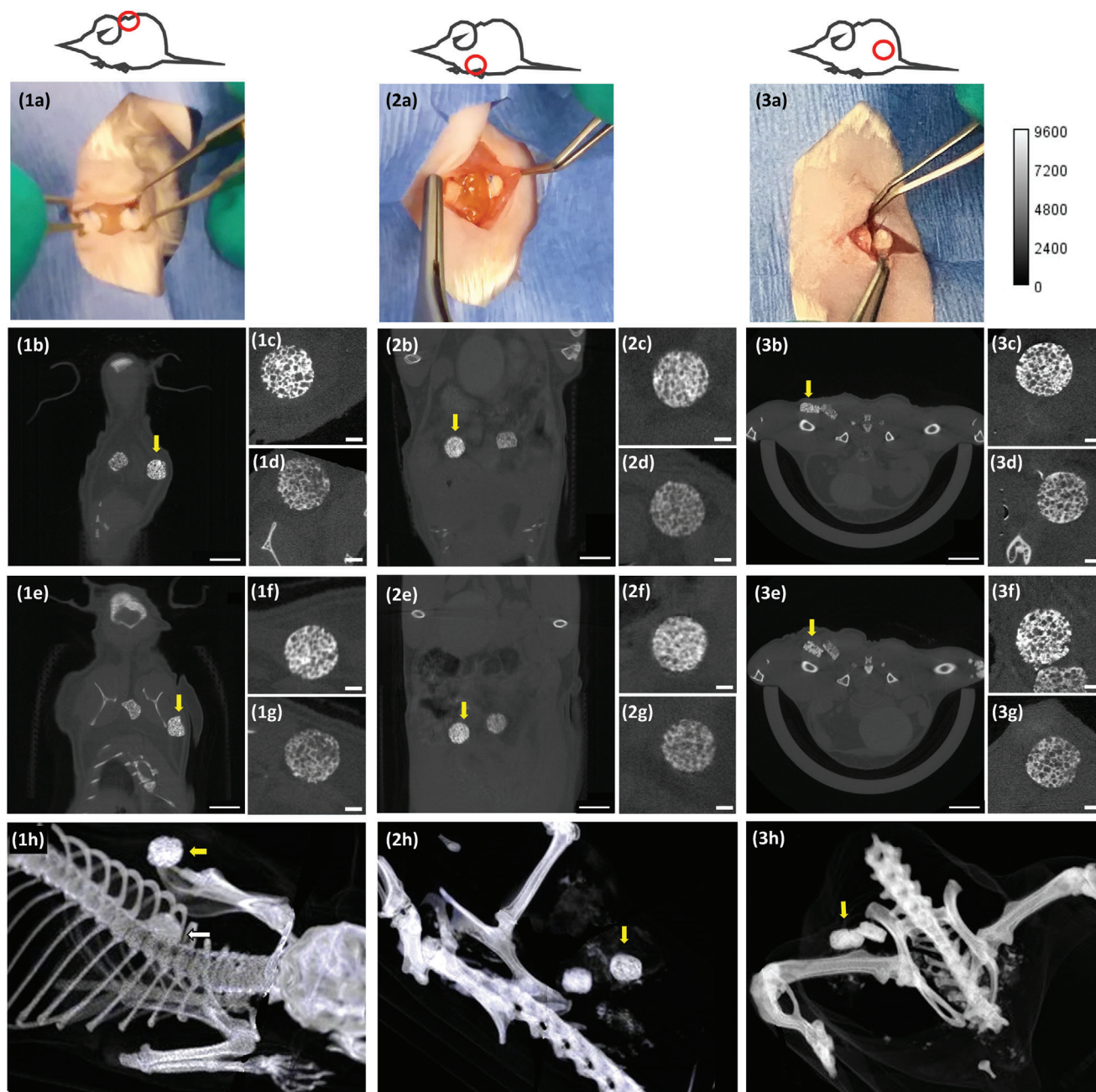


**Figure 6.** In situ monitoring using CT is possible in a variety of locations including 1) subcutaneous, 2) peritoneal, and 3) intramuscular. Implantation of phantoms containing 20 and 30 wt% TaO<sub>x</sub> as viewed a) macroscopically at the time of implantation into mice and via  $\mu$ CT scanning at b–d) day 1 post-implantation and e–h) 5 weeks post-implantation. Resolvable features in the phantoms depended on the scanning resolution, which was affected by involuntary movement (eg., breathing) in some regions: b,e) 90  $\mu$ m, (1c,d, 3c,d, 3f,g): 20  $\mu$ m, (1f,g, 2c,d, 2f,g): 50  $\mu$ m. Movement of the phantoms is noted over time, particularly in the subcutaneous space (3a–h). In (b,e) both phantoms are shown in the same field of view regardless of implanted orientation. Higher resolution images (c–d, f–g) show all phantoms in the same plane; (c,f) 30 wt% TaO<sub>x</sub>, (d,g) 20 wt% TaO<sub>x</sub>. Each implanted phantom was 3 mm diameter  $\times$  1.5 mm thick; yellow arrow marks the phantom incorporating 30 wt% TaO<sub>x</sub> and the white arrow marks the 20 wt% TaO<sub>x</sub>. f) 3D projections of the phantoms and skeletal structure. Scale bar (b,e): 5 mm, (c,d, f,g): 1 mm; the HU window applies to all scans.

stress–strain curve from the first loading cycle. The percentage of deformation was obtained by dividing the phantom thickness after the initial loading cycle by the original thickness  $\times$  100%. The phantom thickness post-loading was determined to be the point at which the force applied to the phantom was greater than 0.02 N during the second loading cy-

cle. After testing, phantoms were removed from the machine, placed in the original microcentrifuge tube, and washed in 1 mL deionized water, shaking at 80 rpm, for 1 h at room temperature. The water was subsequently removed and the phantoms were dried at room temperature before determining the remaining mass. Mechanics and mass loss for PLGA

phantoms were measured at least once per week for up to 20 weeks. Phantoms made from PCL, a non-degrading matrix, were measured once every 2 weeks for 20 weeks.

To calculate mass loss, the initial phantom mass was computed as the difference between the empty microcentrifuge tubes and the microcentrifuge tube + phantom. After mechanical testing, dried phantoms were weighed again and the difference from the empty microcentrifuge weight was taken as the remaining mass.

**Micro-Computed Tomography:** All tomography images were obtained using a Perkin-Elmer Quantum GX. At every time point, groups of three phantoms were imaged at 90 keV, 88  $\mu$ A, with a 25 mm field of view at a 50  $\mu$ m resolution. After the acquisition, individual phantoms were sub-reconstructed using the Quantum GX software to 12–18  $\mu$ m resolution. Phantoms used for serial monitoring were imaged on day 0 prior to hydration for pore size analysis (Supporting Information) and imaged again 24 h after hydration with buffer. Throughout the remainder of the study, all groups were imaged every week after changing the buffer media.

In vivo  $\mu$ CT on mice was performed at 90 keV, 88  $\mu$ A. At each time point, two scans were taken of the phantoms, 1) 72 mm field of view (14 min total scan time) at 90  $\mu$ m resolution and 2) 36 mm field of view (4 min total scan time) at 20–50  $\mu$ m resolution. In the subcutaneous implantation, both phantoms could not be captured in a single higher-resolution scan, so two scans were taken, one centered on each implant. During acquisition, mice were anesthetized using an inhalant anesthetic of 1–3% Isoflurane in 1 L  $\text{min}^{-1}$  oxygen. Mice were scanned immediately post-implantation, on day 1 post-implantation, and at day 7 and week 5 post-implantation. Total cumulative radiation dosage was 14–19 Gy over 5 weeks. Of the total dose, 2.5 Gy were due to low magnification scans that exposed multiple organ systems, but which were below limits established for repeated murine scanning.<sup>[43]</sup> The remainder of the radiation dose (11.5–17.5 Gy) was delivered to local regions around the phantoms. The physiological result of the localized scans was dependent on the sensitivity of surrounding tissues such as adipose tissue or bone marrow.<sup>[44]</sup> In the present study, this was tracked via complete blood count following euthanasia (Table S1, Supporting Information).

**Tomography Image Analysis:** From the tomography scans of phantoms, several parameters were quantified. The gross features of the phantoms (thickness, diameter) were analyzed using Image J. For phantoms with 5 wt% TaO<sub>x</sub>, 50  $\mu$ m scans were used to collect data; 12–18  $\mu$ m sub-reconstructions were used for all other phantoms. Image stacks were opened and rotated, using built-in functions, to measure thickness and diameter in five planes, which were averaged. From the diameter and thickness, a “gross volume” was defined as the volume occupied by a solid cylinder with the corresponding thickness and diameter. In the case of the phantoms, this gross volume consisted of both the polymer volume and the volume of the pores.

Analysis of the polymer matrix component of phantoms with 20 and 40 wt% TaO<sub>x</sub> was performed using custom software developed with MATLAB (v R2021b, Mathworks, Natick, MA) on  $\mu$ CT sub-reconstructions; phantoms with 5 wt% TaO<sub>x</sub> could not be radiographically distinguished from the background. Before segmenting the polymer from the background, the image was preprocessed by using an adaptive histogram equalization technique to enhance contrast.<sup>[45]</sup> After, Otsu's binary segmentation method was used to create a rough mask of the volume.<sup>[46]</sup> An adaptive thresholding method was then employed to segment the polymer within the rough mask from the background.<sup>[47]</sup> The resulting volume was cleaned up using erosion and dilation operations. The program calculated the mean attenuation of the phantom, the volume of the polymer in the phantom, the phantom diameter and thickness, the number of pores, and the average pore diameter. From this, the percent porosity of the phantoms was calculated as the percentage of the gross volume not occupied by the matrix. The percentage difference between the average mass loss and volume of the polymer matrix was also calculated; it was defined as the difference between percentage mass loss and percentage polymer volume divided by the average value of the two metrics. In this case, a positive value corresponded to a lower volume loss than mass loss and a negative value reported a greater mass loss than volume loss.

**Pilot Implantation:** PCL implants containing 20 and 30 wt% TaO<sub>x</sub> nanoparticles were prepared as detailed above. After preparation, phantoms were cut to 3 mm diameter with a biopsy punch and were soaked in 70% ethanol for 2 h. The ethanol was replaced by sterile PBS and sonicated for 5 min, twice, and the implants were left in sterile PBS at 37 °C until implantation.

All procedures were performed in accordance with IACUC-approved protocols and Veterinary guidelines at Michigan State University. BALB/c Mice ( $n = 3$  adult males, 7 months old; Charles River Laboratories) were used for this surgical implantation and  $\mu$ CT imaging pilot study. Each mouse was surgically implanted with two PCL implants containing either 20 or 30 wt% TaO<sub>x</sub> nanoparticles installed adjacent to each other within the single implantation surgical site. The PCL implants were implanted subcutaneously ( $n = 1$  mouse) dorsal-thoracic between the scapulae, intramuscularly ( $n = 1$  mouse) dorsal-medially between the biceps femoris and superficial gluteal muscles, and intraperitoneally ( $n = 1$  mouse) via a ventral midline laparotomy superficial to the liver. Each animal was administered analgesia at least 20 min prior to making the initial incision, including prophylactic Ampicillin (25 mg  $\text{kg}^{-1}$ ; SID) administered S.C., Meloxicam (5 mg  $\text{kg}^{-1}$ ; SID) administered S.C. in the right dorsal lateral flank of the animal, and local infiltration of 2% Lidocaine (diluted to 0.5%) was administered S.C. along the intended incision site just prior to making the cutaneous incision (7 mg  $\text{kg}^{-1}$  Max dose; SID). Animals were anesthetized via inhalant isoflurane (3–4% isoflurane in 0.8–1LPM oxygen for induction) and maintained via inhalant isoflurane during surgery (1–3% isoflurane in 0.8–1LPM oxygen). Supplemental heat was provided via recirculating warm water blankets during anesthesia induction, patient preparation, surgery, and patient recovery. Each scaffold was sutured to surrounding tissue with at least one single interrupted suture using 9-0 PROLENE (Polypropylene) monofilament Suture for in situ location retention. Incision sites were closed in multiple layers where necessary using 5-0 COATED VICRYL (polyglactin 910) Suture and cutaneous layers were closed using 5-0 PDS-II (polydioxanone) Suture. Following animal recovery, Meloxicam (5 mg  $\text{kg}^{-1}$ ; SID) and Buprenorphine (2 mg  $\text{kg}^{-1}$ , BID, every 8–12 h) were administered S.C. in the left or right dorsal lateral flank of the animal for 48 h following surgery. Post-operative clinical observation, body weight assessment, and health score assessment were performed for 7–14 days postoperatively. Animals were scanned with  $\mu$ CT immediately post-implantation, and again on day 1, day 7, and week 5 post-implantation. At termination, animals were sacrificed via CO<sub>2</sub> overdose asphyxiation. Following euthanasia, blood samples were collected for complete blood count (Table S1, Supporting Information).

**Statistics:** Statistics were performed using GraphPad 9.4.1. Mechanical data were analyzed via the non-parametric Kruskal–Wallis test followed by multiple comparisons of the means, using the two-stage step-up method of Benjamini, Krieger, and Yekutieli test, to control the False Discovery Rate. All other data were analyzed via ANOVA, followed by Tukey's multiple comparisons tests. In all cases,  $\alpha < 0.05$  was considered significant, with a 95% confidence interval.

## Supporting Information

Supporting Information is available from the Wiley Online Library or from the author.

## Acknowledgements

The authors would like to thank P. Askeland from the MSU Composite Materials and Structures Center for help with scanning microscopy. This study was funded by the National Institute of Biomedical Imaging and Bioengineering of NIH under award number R01EB029418. The content is solely the responsibility of the authors and does not necessarily represent the official views of the National Institutes of Health.

## Conflict of Interest

The authors declare no conflict of interest.

## Data Availability Statement

The data that support the findings of this study are available from the corresponding author upon reasonable request.

## Keywords

computed tomography, degradation, monitoring, nanoparticles, radiopacity

Received: December 6, 2022

Revised: February 19, 2023

Published online: March 13, 2023

- 
- [1] M. Veletic, E. H. Apu, M. Simic, J. Bergsland, I. Balasingham, C. H. Contag, N. Ashammakhi, *Chem. Rev.* **2022**, 122, 16329.
- [2] J. Wallyn, N. Anton, S. Akram, T. F. Vandamme, *Pharm. Res.* **2019**, 36, 78.
- [3] K. Pawelec, S. Chakravarthy, J. Hix, K. Perry, L. van Holsbeeck, R. Fajardo, E. Shapiro, *ACS Biomater. Sci. Eng.* **2021**, 7, 718.
- [4] Y.-H. Shao, K. Tsai, S. Kim, Y.-J. Wu, K. Demissie, *JNCI Cancer Spectr.* **2020**, 4, pkz072.
- [5] D. A. Szulc, H.-L. M. Cheng, *Macromol. Biosci.* **2019**, 19, 1800330.
- [6] A. Erol, D. B. H. Rosberg, B. Hazer, B. S. Goencue, *Polym. Bull.* **2020**, 77, 275.
- [7] M. E. Mertens, A. Hermann, A. Buehren, L. Olde-Damink, D. Moeckel, F. Gremse, J. Ehling, F. Kiessling, T. Lammers, *Adv. Funct. Mater.* **2014**, 24, 754.
- [8] C. Gil, M. L. Tomov, A. S. Theus, A. Cetnar, M. Mahmoudi, V. Serpooshan, *Micromachines* **2019**, 10, 474.
- [9] J. M. Crowder, N. Bates, J. Roberts, A. S. Torres, P. J. Bonitatibus, *J. Anal. At. Spectrom.* **2016**, 31, 1311.
- [10] J. W. Lambert, Y. Sun, C. Stillson, Z. Li, R. Kumar, S. Wang, P. F. FitzGerald, P. J. Bonitatibus, R. E. Colborn, J. C. Roberts, P. M. Edic, M. Marino, B. M. Yeh, *Radiology* **2018**, 289, 103.
- [11] S. Chakravarty, J. M. L. Hix, K. A. Wiewiora, M. C. Volk, E. Kenyon, D. D. Shuboni-Mulligan, B. Blanco-Fernandez, M. Kiupel, J. Thomas, L. F. Sempere, E. M. Shapiro, *Nanoscale* **2020**, 12, 7720.
- [12] G. Mohandas, N. Oskolkov, M. T. McMahon, P. Walczak, M. Janowski, *Acta Neurobiol. Exp.* **2014**, 74, 188.
- [13] K. Ji, L. Mayernik, K. Moin, B. F. Sloane, *Cancer Metastasis Rev.* **2019**, 38, 103.
- [14] A. Goepferich, *Biomaterials* **1996**, 17, 103.
- [15] F. Alexis, *Polym. Int.* **2005**, 54, 36.
- [16] L. Lu, S. J. Peter, M. D. Lyman, H.-L. Lai, S. M. Leite, J. A. Tamada, S. Uyama, J. P. Vacanti, R. Langer, A. G. Mikos, *Biomaterials* **2000**, 21, 1837.
- [17] M. Bartnikowski, T. R. Dargaville, S. Ivanovski, D. W. Huttmacher, *Prog. Polym. Sci.* **2019**, 96, 1.
- [18] G. Narayanan, V. N. Vernekar, E. L. Kuyinu, C. T. Laurencin, *Adv. Drug Delivery Rev.* **2016**, 107, 247.
- [19] K. M. Pawelec, J. Koffler, D. Shahriari, A. Galvan, M. H. Tuszynski, J. Sakamoto, *Biomed. Mater.* **2018**, 13, 044104.
- [20] S. Pina, V. P. Ribeiro, C. F. Marques, F. R. Maia, T. H. Silva, R. L. Reis, J. M. Oliveira, *Materials* **2019**, 12, 1824.
- [21] T. A. Finamore, T. E. Curtis, J. V. Tedesco, K. Grandfield, R. K. Roeder, *Nanoscale* **2019**, 11, 4345.
- [22] S. M. Forton, M. T. Latourette, M. Parys, M. Kiupel, D. Shahriari, J. S. Sakamoto, E. M. Shapiro, *ACS Biomater. Sci. Eng.* **2016**, 2, 508.
- [23] T. Lex, B. R. Brummel, M. F. Attia, L. N. Giambalvo, K. G. Lee, B. A. Van Horn, D. C. Whitehead, F. Alexis, *Sci. Rep.* **2020**, 10, 1508.
- [24] P. F. FitzGerald, R. E. Colborn, P. M. Edic, J. W. Lambert, A. S. Torres, P. J. Bonitatibus, B. M. Yeh, *Radiology* **2016**, 278, 723.
- [25] A. Carbone, M. Song, K. E. Uhrich, *Biomacromolecules* **2008**, 9, 1604.
- [26] Y. Wong, A. V. Salvekar, K. D. Zhuang, H. Liu, W. R. Birch, K. H. Tay, W. M. Huang, S. S. Venkatraman, *Biomaterials* **2016**, 102, 98.
- [27] K. R. Soneha, G. S. Sailaja, *J. Mater. Chem. B* **2021**, 9, 8569.
- [28] C. Gomez, G. Hallot, S. Laurent, M. Port, *Pharmaceutics* **2021**, 13, 1793.
- [29] J. Wang, L. Helder, J. Shao, J. Jansen, M. Yang, F. Yang, *Int. J. Pharm.* **2019**, 564, 1.
- [30] L. Wu, J. Ding, *Biomaterials* **2004**, 25, 5821.
- [31] Y. K. Reshetnyak, L. Yao, S. Zheng, S. Kuznetsov, D. M. Engelman, O. A. Andreev, *Mol. Imaging Biol.* **2011**, 13, 1146.
- [32] L. V. Deriy, E. A. Gomez, G. Zhang, D. W. Beacham, J. A. Hopson, A. J. Gallan, P. D. Shevchenko, V. P. Bindokas, D. J. Nelson, *J. Biol. Chem.* **2009**, 284, 35926.
- [33] J. H. Jung, M. Ree, H. Kim, *Catal. Today* **2006**, 115, 283.
- [34] K. M. Pawelec, J. Hix, E. M. Shapiro, J. Sakamoto, *J. Mech. Behav. Biomed. Mater.* **2019**, 91, 247.
- [35] C. X. F. Lam, M. M. Savalani, S.-H. Teoh, D. W. Huttmacher, *Biomed. Mater.* **2008**, 3, 034108.
- [36] C. R. Deeken, S. P. Lake, *J. Mech. Behav. Biomed. Mater.* **2017**, 74, 411.
- [37] K. Thiele, C. Perka, G. Matziolis, H. O. Mayr, M. Sostheim, R. Hube, *J. Bone Jt. Surg.* **2015**, 97, 715.
- [38] C. E. Rapier, K. J. Shea, A. P. Lee, *Sci. Rep.* **2021**, 11, 14512.
- [39] D. O. Visscher, E. J. Bos, M. Peeters, N. V. Kuzmin, M. L. Groot, M. N. Helder, P. P. M. van Zuijlen, *Tissue Eng.* **2016**, 22, 573.
- [40] C. M. Murphy, G. P. Duffy, A. Schindeler, F. J. O'Brien, *J. Biomed. Mater. Res., Part A* **2016**, 104A, 291.
- [41] K. Fu, D. W. Pack, A. M. Kibanov, R. Langer, *Pharm. Res.* **2000**, 17, 100.
- [42] N. Hua, J. Sun, *J. Mater. Sci.: Mater. Med.* **2008**, 19, 3243.
- [43] N. Berghen, K. Dekoster, E. Marien, J. Dabin, A. Hillen, J. Wouters, J. Deferme, T. Vosselman, E. Tiest, M. Lox, J. Vanoirbeek, E. De Langhe, R. Bogaerts, M. Hoylaerts, R. Lories, G. Vande Velde, *Sci. Rep.* **2019**, 9, 17598.
- [44] J. Meganck, B. Liu, *Mol. Imaging Biol.* **2017**, 19, 499.
- [45] K. Zuiderveld, in *Graphics Gems* (Eds: P. S. Heckbert), Academic Press, San Diego, CA **1996**, pp. 474–485.
- [46] N. Otsu, *IEEE Trans. Syst. Man Cybern.* **1979**, 9, 62.
- [47] D. Bradley, G. Roth, *J. Graphics Tools* **2007**, 12, 13.